Electroless synthesis of nanostructured nickel and nickel–boron tubes and their performance as unsupported ethanol electrooxidation catalysts

Falk Muench [a,*], Mehtap Oezaslan [b], Markus Rauber [a], Sebastian Kaserer [a], Anne Fuchs [a], Eric Mankel [a], Joachim Brötz [a], Peter Strasser [b], Christina Roth [a], Wolfgang Ensinger [a]

[a] Department of Materials and Geoscience, Technische Universität Darmstadt, Petersenstraße 23, 64287 Darmstadt, Germany
[b] Department of Chemistry, Technische Universität Berlin, Straße des 17. Juni 124, 10623 Berlin, Germany

HIGHLIGHTS

► New electroless plating bath allows fabrication of pure Ni nanomaterials.
► Tubular Ni and Ni–B nanomaterials are obtained by metalization of hard templates.
► 1D Ni catalysts show clearly improved acitivies in ethanol electrooxidation.
► The presence of boron does not hamper the electrocatalytic activity.

GRAPHICAL ABSTRACT
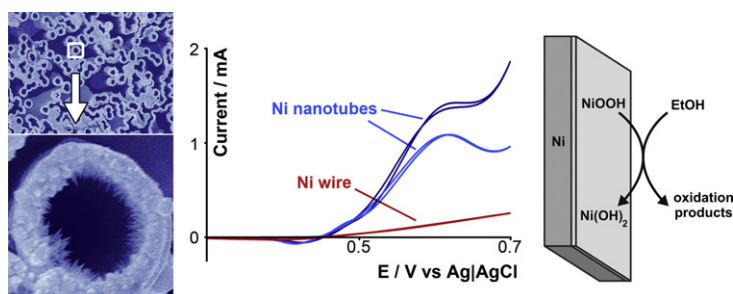
ARTICLE INFO

ABSTRACT

Considering the low abundance of platinum group metals and the high catalytic performance of nickel for the oxidation of small organic molecules, nickel catalysts are promising substitutional materials for direct alcohol fuel cells. Despite the simplicity, good scalability and flexibility of electroless plating, reports on the fabrication of nickel-based catalysts with this method are rare, in particular regarding the deposition of pure nickel. To expand the existing synthetic repertoire, we developed an electroless plating bath allowing the homogeneous deposition of spiky nickel films on very complex shaped substrates. Nanostructured nickel and nickel–boron tubes were obtained by combination of the new and a borane-based plating reaction polymer templates, respectively. The composition, morphology and crystallinity of the products was comprehensively investigated with X-ray photoelectron spectroscopy (XPS), scanning electron microscopy (SEM), transmission electron microscopy (TEM), energy-dispersive X-ray spectroscopy (EDS) and X-ray diffraction (XRD). Finally, the nickel and nickel–boron tubes were applied as unsupported electrocatalysts for the oxidation of ethanol (EtOH) in alkaline environment. Compared to a macroscopic reference, both of the nanostructured catalysts showed improved utilization of high EtOH concentrations and considerably increased oxidation activities, rendering the applied deposition reactions promising routes towards novel catalysts for direct alcohol fuel cells.

1. Introduction

Lately, there is a rising need for cost-efficient energy storage and conversion solutions and a desire to redesign economic processes towards increased sustainability and independence from rare materials. In the course of these developments, common

* Corresponding author. Tel.: +49 6151 166387; fax: +49 6151 166378.
E-mail address: muench@ca.tu-darmstadt.de (F. Muench).

metals are attracting considerable interest as substitutes for expensive catalyst systems. For instance, Fe was used to efficiently generate hydrogen from formic acid [1], Cu was implemented in a room temperature operated borane fuel cell [2], and Ni was applied in the oxidation of small organic molecules such as methanol [3], EtOH [4–7] and glucose [8]. Due to the sluggish alcohol electrooxidation kinetics in acidic electrolytes, much research has been performed on the development of fuel cell setups and novel catalyst systems for the operation in alkaline environment [9,10]. In this reaction type, Ni is an interesting substitutional material for noble metals such as Pt [10].

Nanostructured metal catalysts provide enhanced surface area [2,4,7] and often exhibit improved performance compared to the bulk materials [8]. Among the different classes of metal catalysts, unsupported, highly anisotropic structures such as nanotubes (NTs) or nanowires recently attracted special attention due to their enhanced properties [11–14]. While conventional catalyst designs such as carbon black decorated with metal nanoparticles often suffer from moderate electron transfer and corrosion, one-dimensional metal nanostructures can exhibit excellent conductivity [11,14] and aging resistance [11–13]. Also, NTs have a large and well accessible surface [11–13], allowing excellent mass transport of chemical species between the surrounding medium and the catalyst. Finally, high metal loadings which are needed e.g. for direct alcohol or high performance fuel cells can be effectively obtained with unsupported nanostructures [11,14].

However, special synthetic routes are required to create metal NTs, mostly involving hard [13–17] or sacrificial templates [12] which enforce the uncommon morphology by spatial confinement. In combination with template methods, electroless plating is often used to fabricate complex, arbitrary shaped metal nanostructures [18] and metal NTs [15–17]. This versatile yet surprisingly simple class of wet-chemical metal depositions is based on the autocatalytic, surface-selective reduction of metal precursor solutions. The electrons for reduction are provided by a dissolved chemical agent [15–20], and the reactions can be easily scaled up. No complicated instrumentation is necessary to initiate the continuous metal deposition. A suitable work piece only has to be immersed in an electroless plating bath. The substrates do not need to be conductive, and can be shaped very irregularly [15–18]. However, for the preparation of nanomaterials with this technique, sufficient reaction control and deposition homogeneity are required [21].

Despite the outstanding catalytic performance of tubular metal nanocatalysts [11–13,21] and the effectiveness of Ni catalysts for the electrooxidation of EtOH [4–7] as an important fuel cell reaction for upcoming portable energy applications, Ni NTs have not been tested in alcohol oxidation to date. In addition, there are only very few reports on electroless plating procedures with sufficient nanoscale control to fabricate Ni NTs in porous templates [15,16], and they rely on hypophosphite or aminoboranes as the reducing agents. The insertion of heteroatoms (P, B) by these conventional reducing agents [15,16,22,23] can be detrimental to the properties of the resulting materials. For instance, the presence of boron clearly reduces the ductility of Ni [19] as well as its catalytic performance in hydrogenation reactions [22].

In this work, we present a route to overcome the lack of electroless plating protocols suitable for the fabrication of pure Ni nanomaterials with complex morphologies. Ni NTs were synthesized with a newly developed plating bath based on the clean reducing agent, hydrazine, and the previously reported dimethylaminoborane (DMAB) [23]. To the best knowledge of the authors, this is the first report of the synthesis of tubular structures in porous hard templates consisting of pure Ni. Finally, the two Ni NT catalyst types were applied in the electrooxidation of EtOH to evaluate their catalytic potential in dependence on their nanostructure and composition.

2. Experimental

2.1. General, chemicals

Glassware was cleaned with nitric acid prior to use. All solutions were freshly prepared. Milli-Q water (>18 MΩ) was employed in all procedures. The following chemicals were applied without further purification: 2-chlorophenol (Aldrich, 98%); $AgNO_3$ (Grüssing, p.a.); CH_2Cl_2 (Sigma Aldrich, puriss. p.a.); borane dimethylamine complex (Fluka, purum); EtOH (Labor Service GmbH, p.a.); iminodiacetic acid (Fluka, purum); methanol (Aldrich, 99.8%); NaOH solution 32% in water (Fluka, puriss. p.a.); Ni wire (Aldrich, ≥99.9% trace metal basis); $NiSO_4 \cdot 6H_2O$ (Sigma–Aldrich, puriss. p.a.); $N_2H_4 \cdot 1H_2O$ solution 80% in water (Merck, for synthesis); NH_3 solution 33% in water (Merck, puriss.); $SnCl_2 \cdot 2H_2O$ (Sigma–Aldrich, ACS reagent); sodium citrate tribasic dihydrate (Sigma–Aldrich, puriss. p.a.); trifluoroacetic acid (Riedel-de Haën, >99%).

2.2. Fabrication of Ni nanostructures

The synthetic steps involved in the Ni NTs fabrication are summarized in Fig. 1, beginning with the template preparation. At first, polycarbonate (PC, Makrofol® from Bayer Material Science AG) and polyethylene terephthalate (PET, Hostaphan® from Hoechst) foils (nominal thickness: PC 30 μm, PET 36 μm) were irradiated with Au ions (energy = 11 MeV per nucleon, fluence = 1×10^8 ions cm^{-2}) at the GSI Helmholtz Centre for Heavy Ion Research. The PET foil was irradiated with UV light (Privileg UVA lamp, 105 W, 1 h irradiation per side) to improve etchability. Subsequently, the polymer foils were etched in stirred NaOH solutions (50 °C, PC: 6 mol L^{-1} NaOH, PET: 4.8 mol L^{-1} NaOH), leading to the selective removal of the ion tracks and the formation of cylindrical channels inside the foils. The diameter of the channels was adjusted by variation of the etching time [24]. The as-prepared templates were washed with water and dried. Prior to electroless plating, the templates were activated with a thin layer of Ag nanoparticles which act as nuclei to initiate the metal deposition
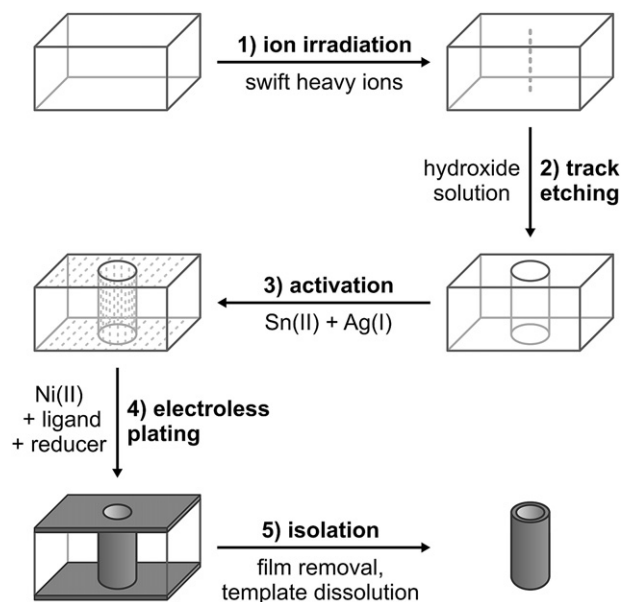

Fig. 1. Sketch of the synthetic steps involved in the fabrication of metal NTs by combining electroless deposition with ion track etched polymer templates.

reaction [17]. Briefly, the polymer surface was covered with reducing species by immersing the template in a solution of $SnCl_2$ and trifluoroacetic acid in methanol–water. After the transfer to an ammoniac solution of $AgNO_3$, small Ag nanoparticles were formed on the template surface. Subsequently, the templates were washed with EtOH and water and transferred to the electroless plating solutions. The plating solution for pure Ni consisted of 0.05 mol L^{-1} $NiSO_4$ (metal source), 0.1 mol L^{-1} iminodiacetic acid (ligand), 0.25 mol L^{-1} NaOH (pH adjustment) and 1.0 mol L^{-1} N_2H_4 (reducing agent). The borane-based plating bath contained 0.1 mol L^{-1} $NiSO_4$ (metal source), 0.1 mol L^{-1} citrate (ligand) and 0.1 mol L^{-1} DMAB (reducing agent). After the deposition of Ni, the metal surface films were removed with abrasive paper. Depending on the polymer type, the templates were dissolved with dichloromethane (PC) or hot o-chlorophenol (PET; special carefulness is required due to the intense stench of the solvent). The freed metal structures were cleaned by centrifugation and redispersion in fresh solvent.

2.3. Characterization

SEM (JEOL JSM–7401F, 5–10 kV acceleration voltage): Template-freed nanostructures were collected on Si wafer pieces sputter-coated with Au, while the Ni-covered PET template was examined with the polymer. TEM (FEI TECNAI G2 20 S_TWIN, LaB_6 cathode, GATAN MS794 P CCD camera, 200 kV acceleration voltage): The tube-containing templates were embedded in Araldite 502$^{©}$ (polymerization at 60 °C for 24 h) and examined as ultrathin sections (70 nm, Reichert-Jung Ultracut E ultramicrotome, DKK diamond knife). The ultrathin samples were sputtered with carbon before the structural and chemical investigations in the TEM. The EDS measurements were carried out in the TEM microscope. XRD (Stoe Stadi P): The X-ray diffraction investigations were performed with the wavelength of Mo $K_{\alpha 1}$ using a Ge(111) monochromator on the primary side. The Ni tubes were dispersed in isoamyl acetate:collodium = 8:2, glued between two acetate foils and measured in transmission geometry. XPS (VG Escalab 250 spectrometer using monochromatic Al K_α radiation with an energy of hv = 1486.6 eV and a line width of $\Delta(hv) \leq 0.4$ eV): The spectra were recorded in constant analyzer energy mode using pass energies of 10 eV for the detail spectra of individual emission lines. The measurements were carried out at a base pressure of 2×10^{-7} Pa and room temperature. The binding energy scale of the detail spectra is calibrated using clean sputtered metal surfaces (Ag, Cu). Hence the origin of this scale corresponds to the Fermi energy of the sample.

2.4. Electrochemistry

For the electrochemical measurements, a Gamry Reference 600™ potentiostat was used in a three electrode setup involving a Pt foil (counter electrode), a 1.6 cm^2 glassy carbon disc (working electrode) and an Ag|AgCl reference electrode (in 3.0 M KCl). All potentials mentioned below are given in relation to the Ag|AgCl reference electrode. To prepare the catalytic thin films on the working electrode, suspensions of the NTs prepared by dissolution of the templates in dichloromethane were dropped on the electrode surface and left to dry in air, leading to Ni nanotube loadings of approx. 0.033 mg cm^{-2} (Ni–B NTs) and 0.12 mg cm^{-2} (Ni NTs). 0.1 mol L^{-1} NaOH solutions with different concentrations of absolute EtOH were used as electrolyte. Before the measurements, the electrolyte was purged with nitrogen for 15 min. To avoid disturbance, the nitrogen stream was led above the electrolyte's surface during the electrochemical experiments. A potential range from 0 mV to 700 mV vs. Ag|AgCl was chosen. In this potential range, the GC electrode used to contact the Ni NTs does not significantly contribute to the measured currents and thus can be neglected. Also, Ni bulk oxidation is suppressed by using this moderate upper potential limit [25]. Relatively large structures were chosen because of their good mechanical stability and adhesion to the electrode.

3. Results and discussion

3.1. Development of an electroless plating bath for the synthesis of nanostructured Ni tubes

If pure Ni deposits are desired, hydrazine is the favored reducing agent in electroless Ni plating [19,26–28]. Due to the high pH values required for effective hydrazine oxidation [29] and the low solubility of Ni hydroxide, relatively strong complexing agents have to be introduced to suppress the formation of precipitates. In the case of electroless plating of pure Ni, ethylenediaminetetraacetic acid (EDTA) is frequently used [26,27]. Based on the slow and unreliable deposition behavior of a plating bath solely utilizing EDTA [26], lactic acid was introduced as an auxiliary reagent [26,27]. However, irregularities such as unequal film thicknesses or porosity were still observed in the Ni deposits [26,27]. These synthetic restraints obstruct the fabrication of sophisticated, regularly shaped nanomaterials.

As we encountered similar difficulties in the electroless plating of Ni nanostructures from EDTA baths, a new plating procedure for Ni was developed. Instead of using the strong ligand EDTA in conjunction with a second reagent which accelerates the reaction [26], iminodiacetic acid (IDA) was chosen as a chemically comparable but weaker ligand. Like EDTA, IDA belongs to the class of polyamino carboxylic acids. These polydentate ligands form chelate complexes with metal cations, and the corresponding complex formation constants usually increase with the number of binding sites per molecule. Compared with EDTA, the tridentate IDA only has half as much ligand functionalities (EDTA: 2 amine groups, 4 carboxylic acid groups; IDA: 1 amine group, 2 carboxylic acid groups). Due to the lower complex formation constant and the less bulky structure of IDA, its presence should lead to a decreased thermodynamic and kinetic stabilization of Ni(II) towards reduction. In accordance with this expectation, facile Ni deposition is achieved with the new plating bath at an elevated temperature of 70–80 °C.

To obtain Ni NTs, ion track etched polymer membranes were used as substrates for electroless plating. These templates contain cylindrical channels which are fabricated by selectively etching out linear damage zones resulting from irradiation with heavy ions [24]. Electroless deposition on the channel walls leads to the formation of tubular metal structures. In our case, polyethylene terephthalate (PET) was chosen as the polymer type for the deposition of pure Ni due to its high chemical stability, allowing it to endure the relatively aggressive plating conditions (high pH, increased temperature, presence of hydrazine).

Representative electron micrographs of the obtained Ni structures are displayed in Fig. 2. In good agreement with the nominal template thickness, the tubes are circa 36 μm long. Electroless Ni deposition on PET membranes with a large channel diameter of 1.3–1.4 μm interestingly did not yield individual tubes, but arrays in which the tubes are connected by sheet-like structures oriented parallel to the template surface (Fig. 2A). The formation of flat, hollow structures in addition to cylindrical channels is typical for ion track etched PET [30]. If a sufficient channel density and cavity size is given, molding with Ni leads to the formation of free-standing assemblies. To demonstrate the possibility to vary the diameter of the channels within the templates and to achieve smaller structures, Ni tubes of 0.4 μm diameter were deposited in a PET template fabricated with reduced track etching time (Fig. 2B).
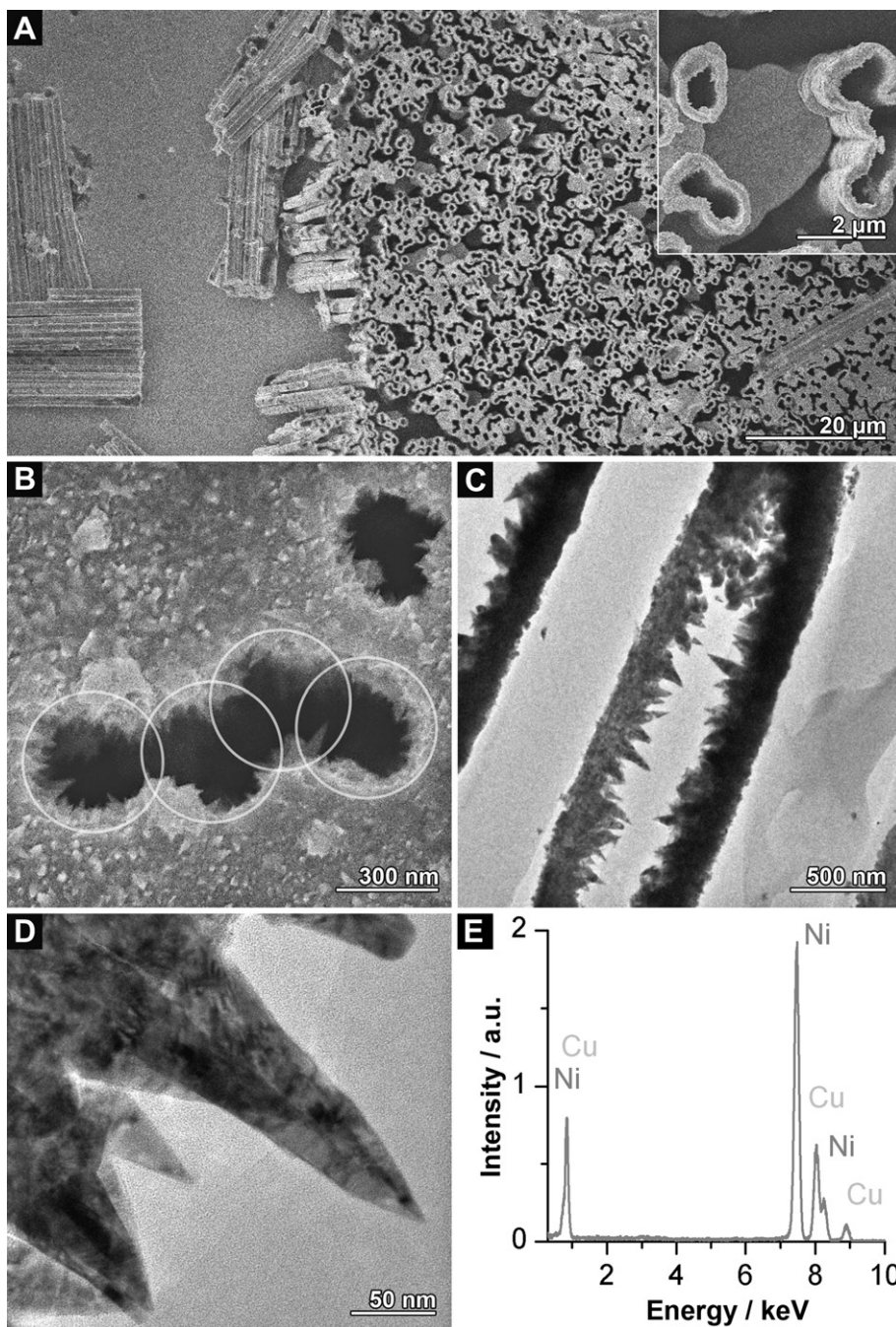
Fig. 2. Electron microscopical analysis of the Ni nanostructures obtained with the new Ni plating bath. A) SEM image of a block of interconnected Ni NTs (the Ni surface film and the polymer were previously removed). The inset shows one of the sheet-like structures which link the tubes. B) SEM image of a Ni surface film including Ni NT openings of approximately 400 nm diameter. Four etched ion tracks are partly merged and form a larger tube (see circles). C) TEM image of a Ni tube cross section. D) Magnified TEM image of the thorn-like structures on the interior Ni walls. E) EDS spectrum of the Ni structures.

The formation of a dense and homogeneous Ni deposit on the outer template surface (Fig. 2B) indicates the suitability of the plating protocol for the creation of two-dimensional films. The thickness of the resulting Ni films and derived nanostructures (e.g. the tube walls) can be easily adjusted by variation of the plating time. As can be seen in SEM images with higher magnification (Fig. 2B), the deposited Ni films have an intensely roughened surface covered with thorn-like structures. For a more detailed analysis of the film nanostructure, TEM measurements on Ni NT cross-sections were performed (Fig. 2C,D). The spiky protrusions vary in size, shape and

orientation, but preferentially grow vertical to the film surface and can reach lengths of more than 150 nm (Fig. 2D). Aside from the TEM measurements, EDS was performed to investigate the purity of the NTs. Apart from Cu signals stemming from the TEM grid, only Ni could be detected in the material (Fig. 2E).

To investigate the surface composition of the Ni NTs, XPS measurements were performed (see Fig. 3A). For convenience, the results of the XPS fits are summarized in Table 1. The XP detail spectrum of the Ni 2p 3/2 emission line was fitted with six peaks which were assigned to three different oxidized Ni species
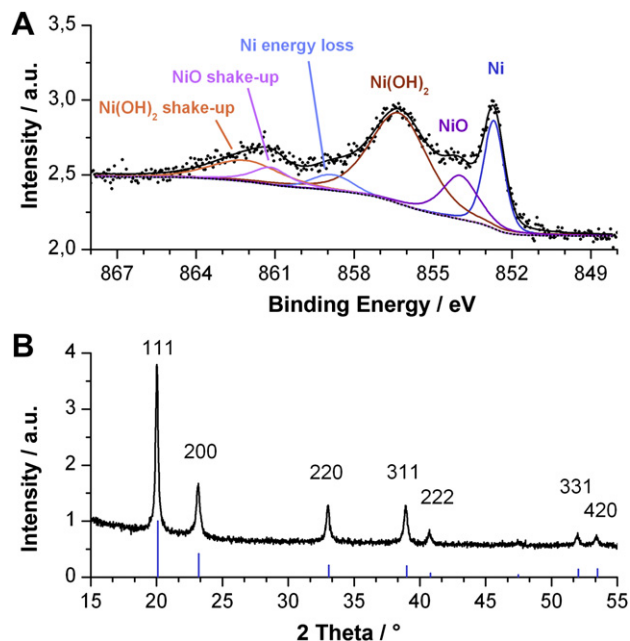
Fig. 3. XPS and XRD characterization of the Ni NTs. A) XP detail spectrum of the Ni 2p 3/2 region. B) XRD pattern of Ni NTs with fcc Ni reference.

(Fig. 3A). Approaching to higher binding energies, the first peak at 852.7 eV was associated with pure metallic Ni. The following two peaks were correlated to oxidized Ni in the form of NiO (854.0 eV) and Ni(OH)$_2$ (856.3 eV). All experimentally observed energy values agree well with those found in the literature (Ni: 852.7 eV [31], 852.9 eV [32]; NiO: 854.1 eV [31], 854.5 eV [32]; Ni(OH)$_2$: 855.9 eV [31], 856.6 eV [32]). At higher energies, additional intensity was detected which was fitted with three peaks: A Ni energy loss peak (858.8 eV; literature: 858.8 eV [31]) and electron shake-up/multielectron excitation peaks corresponding to NiO (861.2 eV; literature: 861.7 eV [31]) and Ni(OH)$_2$ (862.1 eV; literature: 862.4 eV [31]).

The crystallinity of the template-free Ni NTs was examined with XRD (see Fig. 3B). All reflexes in the XRD pattern correspond to elemental Ni and indicate a good crystallinity (Fig. 3B), and no additional reflections of crystalline NiO and Ni(OH)$_2$ species were detected. This result is in accordance with other studies on the hydrazine-based electroless deposition of Ni [20,27,28] and can be explained by a large excess of metallic Ni in the nanostructures, e.g. in the case of full reduction of the material during synthesis and only slight surface oxidation after exposition to ambient conditions. Alternatively, it is possible that the oxidized Ni species found by XPS are amorphous and thus cannot be detected by means of XRD. However, the harsh reducing conditions and the presence of relatively strong ligands render the precipitation of larger amounts of oxidized Ni during the synthesis unlikely.

Table 1
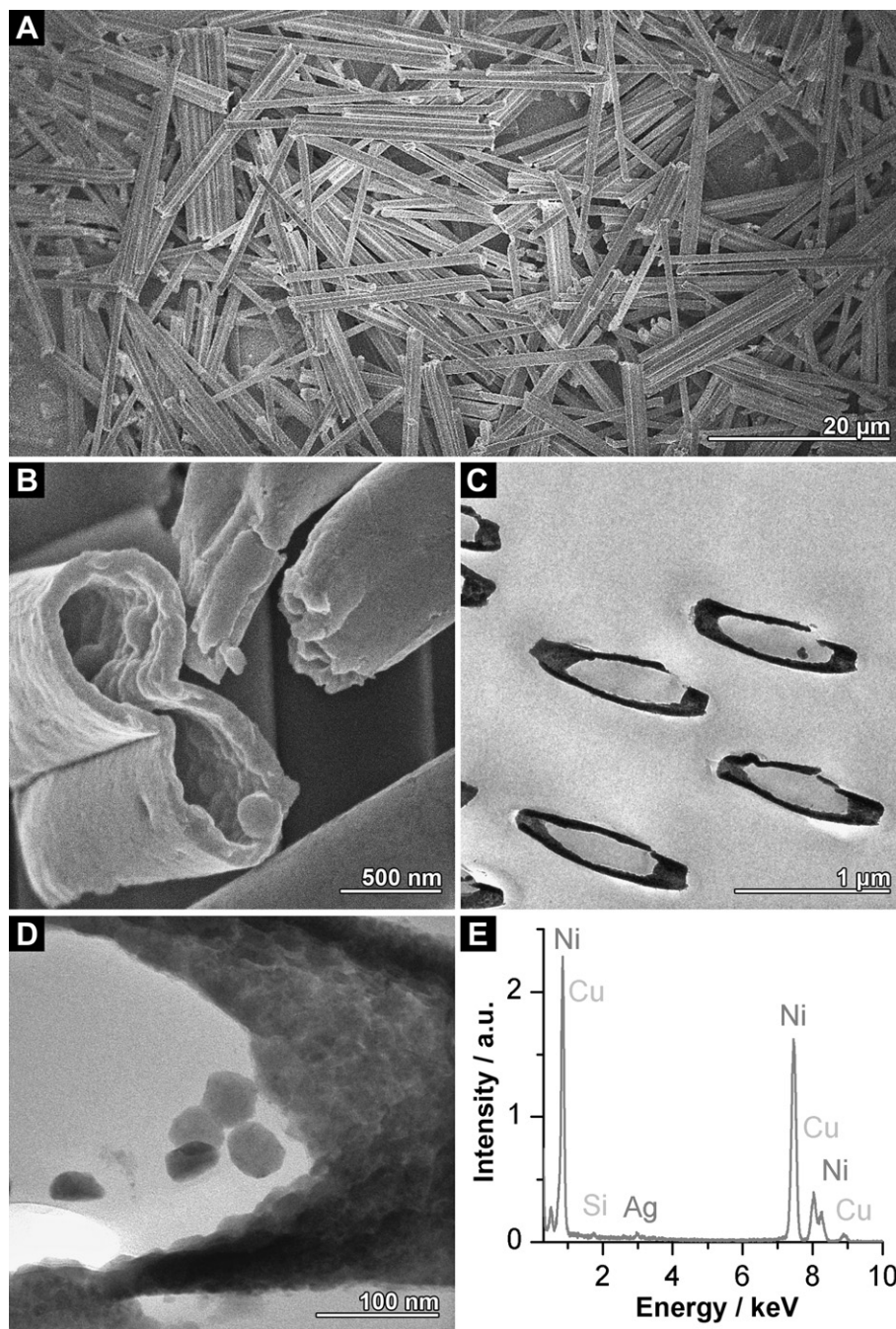Fitted XPS emission line positions and attributed chemical species (Ni NTs).

Emission line	Binding energy/eV	Attributed species	Relative intensity/%
Ni 2p 3/2	852.7	Ni	20
	854.0	NiO	15
	856.3	Ni(OH)$_2$	39
	858.8	Ni (energy loss)	5
	861.2	NiO (multielectron excitation)	14
	862.1	Ni(OH)$_2$ (multielectron excitation)	7

3.2. Fabrication and characterization of Ni–B NTs

In agreement with the highly efficient oxidation of DMAB on Ni [29], Ni deposition from the DMAB-based electroless plating bath could be performed at room temperature. Due to the mild reaction conditions and the simple removability of the polymer, ion track etched polycarbonate templates were applied for the fabrication of Ni–B NTs.

In Fig. 4, electron micrographs of the Ni–B NTs are shown. The resulting tubes exhibited an average length and diameter of 23 μm and 0.9 μm, respectively (Fig. 4A,B). Compared to the Ni NTs synthesized with hydrazine (Fig. 2), the surface of the Ni–B NTs was smoother, and no thorn-like structures were found on the inner tube walls (Fig. 4B). The very uniform film structure facilitates the formation of thin-walled structures and allowed the deposition of NTs even in templates with narrow pores of 200 nm diameter. TEM analysis of thin-walled NTs was performed to obtain more information about the deposit nanostructure (Fig. 4C,D). In contrast to the TEM measurements performed in Fig. 2, the sample was cut perpendicular to the tube axis. Due to the angular cutting of the template, the tubes appear as elliptical rings (Fig. 4C). In magnified images of the NT walls it can be seen that the Ni–B film is composed of grains with the size of few 10 nm (Fig. 4D). By means of EDS, mostly Ni was found in the nanostructures. The Cu and Si signals relate to the TEM grid and the embedding resin, respectively. The expected incorporation of boron from the reducing agent could not be verified by EDS due to its low atomic number. In addition, traces of Ag were found in the nanostructures, stemming from the catalytic nuclei introduced in the template pretreatment. As Ni is less noble than Ag, the Ag nuclei did not take part in exchange reactions [17] and remained in the Ni deposit. The fact that no Ag could be detected in the Ni NTs by EDS (Fig. 2E) is probably related to the larger excess of Ni due to the higher Ni film thickness in this case. XPS confirmed the presence of Ag also in this sample. Concerning the performance of the nanostructures in the EtOH oxidation in the following section, it is unprobable that the Ag particles embedded in the NTs contribute because this metal is inactive in this reaction [33].

For chemical analysis of the Ni–B NTs and the verification of the boron incorporation, XPS measurements were performed. The summarized results are found in Table 2. XPS spectra of the Ni–B NTs revealed the presence of metallic Ni (852.8 eV) and an oxidized Ni species at 856.4 eV on the surface of the Ni–B NTs. Like in the case of the Ni NTs (Fig. 3A), the latter peak was assigned to Ni(OH)$_2$ (Fig. 5A). No significant contribution of NiO was found. Both peak positions are very similar to those obtained for the Ni NTs. Apparently, the presence of B did not cause to a significant shift of the Ni binding energies (compare Figs. 3A and 5A), which is supported by similar results for Ni–B alloys [34,35]. In analogy to the Ni NTs, the remaining intensity at higher binding energies was fitted with two peaks associated with additional signals stemming from Ni (energy loss, 859.1 eV) and Ni(OH)$_2$ (electron shake-up, 862.2 eV). In addition, B could be detected on the surface of the tubes (Fig. 5B). In the B 1s detail spectrum, a peak corresponding to boride [36] was found at 188.2 eV next to an oxidized B species at 192.1 eV which is likely present in the form of B$_2$O$_3$ or Ni borates [34–36]. In contrast to the Ni NTs, very broad reflexes were found in the XRD pattern (Fig. 5C), indicating a semi-amorphous character of the deposit as it is typical for Ni films obtained from DMAB-based deposition baths [23]. The diffractogram could not be explained with Ni alone, as can be seen by the presence of a shoulder on the left side of the first signal at approx. 20° and the position of the second signal at approx. 35°. Although it is impossible to determine the exact phase composition, borides are probably present (e.g. in the form of Ni$_2$B or Ni$_3$B), which also is in agreement with previously published results for electroless Ni–B films [23].

Fig. 4. Electron micrographs of the Ni–B NTs obtained with the reducing agent DMAB. A) SEM image of a field of randomly oriented template-freed Ni–B tubes. B) Magnified SEM image of tube openings. The deformation of the structures is due to the forces occurring during surface film removal. C) TEM image of the cross-section of Ni–B tubes. D) Magnified TEM image of a Ni–B tubes. The cutting procedure led to the translocation of grain-like structures from the tube wall. E) EDS spectrum of the Ni–B NTs.

Table 2
Fitted XPS emission line positions and attributed chemical species (Ni–B NTs).

Emission line	Binding energy/eV	Attributed species	Relative intensity/%
B 1s	188.2	Boride	38
	192.1	B^{3+}	62
Ni 2p 3/2	852.8	Ni	49
	856.4	$Ni(OH)_2$	36
	859.1	Ni (energy loss)	8
	862.2	$Ni(OH)_2$ (multielectron excitation)	7

3.3. Application of the Ni NTs as unsupported electrocatalysts

Prior to the evaluation of the performance of the Ni and Ni–B NTs as EtOH oxidation electrocatalysts, cyclic voltammograms (CVs) were recorded to examine their electrochemical behavior in the alkaline electrolyte. Besides the two NT types, a commercially available Ni wire was used as a macroscopic reference material.
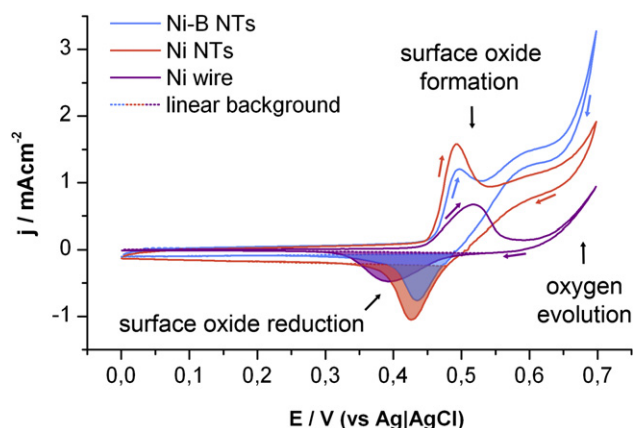
To ensure the comparability of the Ni structures in the preceding electrocatalysis experiments, surface normalization was required. Whereas other metals such as Pt allow a reliable determination of
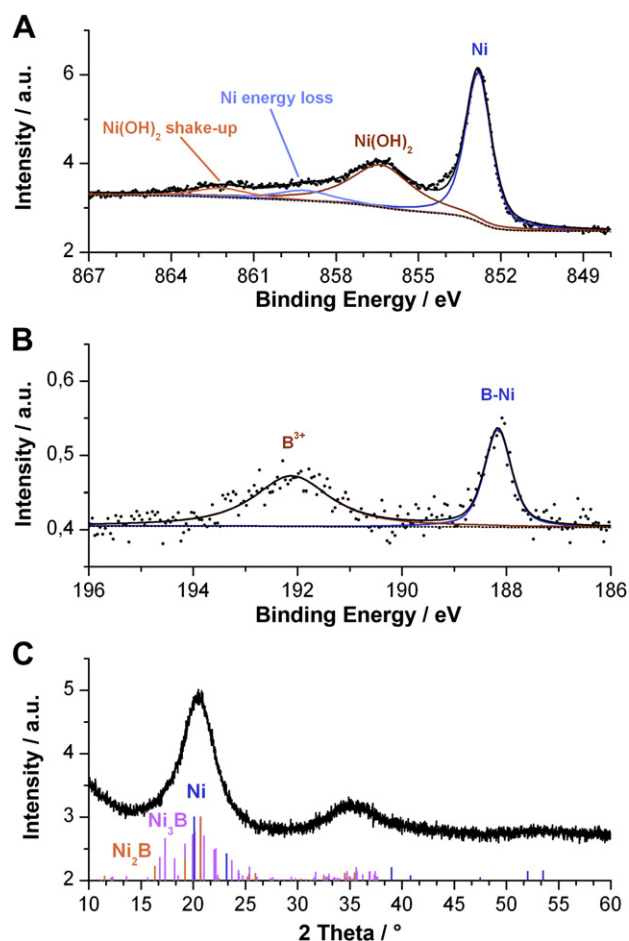
Fig. 5. XPS and XRD characterization of the Ni–B NTs. A) XP detail spectrum of the Ni 2p 3/2 region. B) XP detail spectrum of the B 1s region. C) XRD pattern with corresponding reflex positions of Ni, Ni₃B and Ni₂B references.

Fig. 6. CVs of the three Ni materials recorded with a scan rate of 50 mV s⁻¹ in 0.1 mol L⁻¹ NaOH. Three potential regions and the corresponding electrochemical processes are marked. As a guide to the eye, the shaded regions indicate the integrals of the NiOOH reduction peaks used for normalization. Linear extrapolations of the cathodic scans (0–0.2 V) were used to determine the background (dotted lines).

the electrochemically active surface area (e.g. by the adsorption and desorption of hydrogen), the analog measurements on Ni materials are difficult to analyze due to the following reasons. In the common potential range of hydrogen oxidation Ni already forms oxygen-containing species [25]. Furthermore, the hydrogen stripping for Ni strongly depends on the applied electrochemical conditions [25]. Considering the anodic scan of Ni electrodes in alkaline electrolyte, several processes such as the formation of different surface oxides [25,31] and oxygen evolution [37] overlap. However, the peak in the cathodic scan related to the reduction of Ni surface oxides is usually well separated from other signals [37] and therefore allows facile determination of the charge of this redox transition. As the Ni surface oxide formation/reduction is a fast and reversible process whose charge corresponds to a conversion in the range of a monolayer [38], the reduction peak can be used for the estimation of a catalysts surface area.

Following this concept, we integrated the surface oxide reduction peaks of the three catalysts. To exclude capacitive currents, backgrounds which were obtained by linear regression of the cathodic scans from 0 V to 0.2 V were subtracted from the measured curves. With the obtained reduction charges and the surface area of the Ni wire, the surface areas of the NT samples were determined, and current densities were provided for all Ni structures. The results are shown in Fig. 6. Clearly, the anodic peaks including surface oxide formation and oxygen evolution overlap and are difficult to analyze, while the cathodic peaks are isolated.

Usually, the surface oxide redox couple is interpreted as a transition between superficial, three-valent Ni oxyhydroxide and two-valent Ni hydroxide [10,38] (eq. (1)):

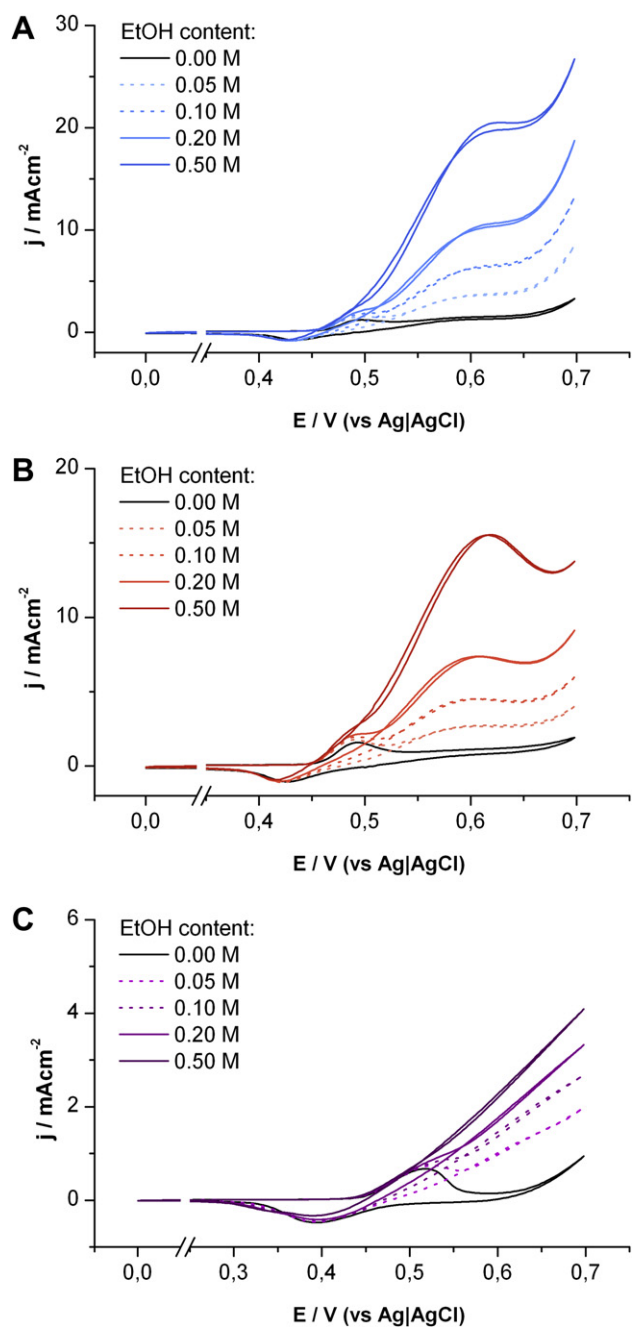$$Ni(OH)_2 + OH^- \rightarrow NiOOH + H_2O + e^- \qquad (1)$$
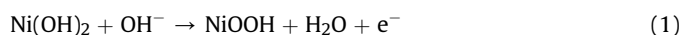
For all three tested Ni catalyst materials, these current peaks appear at approx. 0.5 V in the anodic and 0.4 V in the cathodic scan. In the case of the two Ni NT catalyst types, the differences between the potentials of the redox couple peaks are close to the value of 59 mV as expected for a reversible one-electron process (Ni–B NTs: 62 mV; Ni NTs: 66 mV), while the potential difference of 125 mV for the Ni wire suggests a more inhibited conversion of the electroactive species. Furthermore, both Ni NT catalysts exhibit additional anodic currents at potentials of approx. 0.6 V in which the CV of the Ni wire approaches a low limiting current. As Ni(OH)₂ and NiOOH each exist in two forms (α-Ni(OH)₂, β-Ni(OH)₂, β and γ Ni oxyhydroxide [31]), shoulders in the surface oxide formation peak at higher potentials were explained by the formation of surface oxyhydroxides evolving from the different hydroxides [31]. Apparently, these contributions are more pronounced in the case of the NT catalysts. This observation is in agreement with a study on the electrochemical properties of macroscopic Ni foams. Here, a distinct shoulder at higher potentials was observed only after long-term cycling [31]. Approaching 0.7 V, additional oxidation currents are found on all Ni structures, which can be related to the evolution of oxygen [37]. This reaction predominantly occurs on the Ni NT catalysts.

In a second step, CVs of the three Ni catalysts were recorded with different concentrations of EtOH in alkaline environment (Fig. 7). As supposed by Fleischmann et al. [38], the formed Ni oxyhydroxide is the active species in the oxidation of organic compounds on Ni (see eq. (2)).

$$NiOOH + \text{organic compound} \rightarrow Ni(OH)_2 + \text{oxidation product} \quad (2)$$
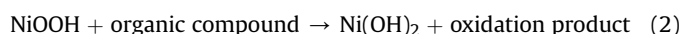
In the case of the two Ni NT catalyst types (Fig. 7A,B), a strong increase of current density was observed with rising EtOH content, whereas the increase of the current density is less pronounced for the Ni wire (Fig. 7C). Comparison of the CVs in the presence and absence of EtOH clearly indicates that the additional anodic currents arise from alcohol oxidation (Fig. 7). Especially at high EtOH concentrations, the NT catalysts show a distinct oxidation

Fig. 7. CVs of the different Ni-based catalysts with different concentrations of EtOH (scan rate: 50 mV s^{-1}) in 0.1 mol L^{-1} NaOH. A) Ni−B NT catalyst. B) Ni NT catalyst. C) Ni wire as reference catalyst.

Table 3
Performance parameters of the different Ni catalysts based on the current densities found at the potential of 0.6 V for an EtOH concentration of 0.5 mol L^{-1} in the anodic scan.

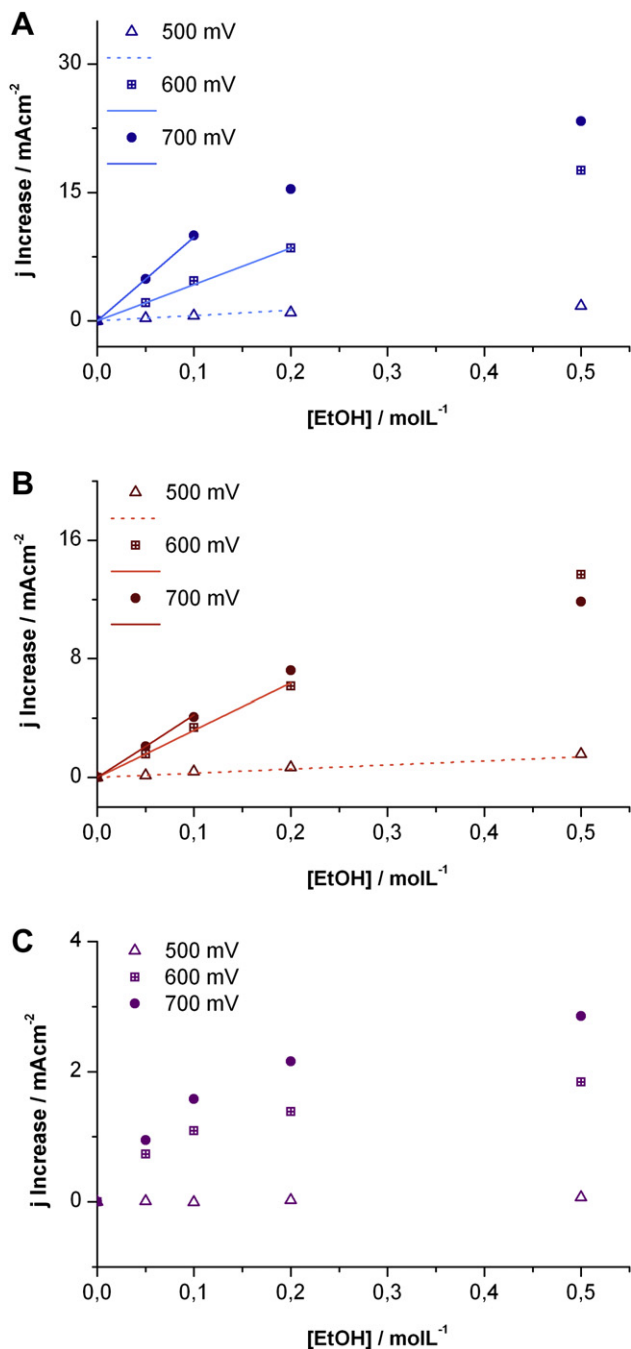| Catalyst	Specific activity/mA cm$^{-2}_{geo}$	Mass activity/mA mg
Ni−B NTs	19.2	430
Ni NTs	14.8	330
Ni wire	2.18	0.0098

established current densities in dependence on the EtOH concentration for three potentials (0.5, 0.6 and 0.7 V). The linearity of the electrochemical response to EtOH addition was evaluated by extrapolation of the current increase between 0 and 0.05 mol L^{-1} EtOH. From a catalytic point of view, this investigation is interesting as the linear range corresponds to the diffusion-controlled reaction regime and thus provides information of the performance of the EOR. In addition, direct alcohol fuel cells are usually operated at high alcohol concentrations [10,39]. Therefore, the efficient utilization of high alcohol contents is an important performance parameter for corresponding catalysts [39].

As can be seen in Fig. 8A, the Ni−B NT catalyst shows the strongest current increase at all potentials. Although the EtOH oxidation already occurs at 0.5 V, the reaction is markedly accelerated at 0.6 and 0.7 V. This can be explained by a more effective re-oxidation (eq. (1)) of EtOH-reduced surface hydroxide (eq. (2)) at high overpotentials. The best linear relationship between the alcohol concentration and the current increase was found for EtOH concentrations between 0 and 0.2 mol L^{-1} at 0.6 V. The Ni NT catalyst shows a very similar behavior with slightly reduced current increase (Fig. 8B). However, opposed to the other two catalysts, a linear relationship between EtOH concentration and current was found over the whole concentration range at a potential of 0.5 V. The Ni wire catalyst did not significantly respond to the variation of the EtOH concentration at a potential of 0.5 V (Fig. 8C). Furthermore, the background-corrected currents were much lower at all potentials, and stronger saturation with respect to increasing EtOH concentration was observed (Fig. 8C). For instance, at a potential of 0.6 V and 0.5 mol L^{-1} EtOH, the current increase of the Ni and the Ni−B NT catalysts was 7 times and 10 times higher than that of the Ni wire, respectively.

The excellent EOR performance of the two Ni NT catalysts is attributed to several properties. First, the surface of the nanostructures is easily oxidized, as can be seen by the reversible redox behavior indicated by the small potential difference of the oxidation and reduction peaks (Fig. 6) and the fast re-oxidation of the surface in the presence of EtOH (Figs. 7 and 8). This is a prerequisite for efficient EtOH conversion according to eq. (2). Also, the alcohol-oxidation related peak aside the first, small anodic signal caused by NiOOH formation is located at relatively low potentials of about 0.6 V (Fig. 7A,B). Other nanostructured Ni catalysts require potentials of 0.72 V (Ni−NP covered carbon NTs; 1.0 mol L^{-1} NaOH + 0.5 mol L^{-1} EtOH, calomel electrode [4]; the higher NaOH concentration should enhance the oxidation reaction [3]), approx. 0.7 V (Ni-seeded carbon NTs; 0.1 mol L^{-1} NaOH + 0.2 mol L^{-1} EtOH [40]) or 1 V (Ni−NP covered carbon NTs; 0.1 mol L^{-1} NaOH + 0.03 mol L^{-1} EtOH, calomel electrode [7]) to reach similar maxima. The high reactivity of the Ni and Ni−B NTs ensures fast EtOH conversion and a linear response even at elevated EtOH concentrations. For instance, for a Ni NP decorated, boron doped diamond electrode a linear response was reported for EtOH contents up to 0.028 mol L^{-1} [5].

The good electrochemical utilization of high EtOH concentrations is important for the application in direct alcohol fuel cells. As the Ni−B NT catalyst is the most effective of the three presented catalyst

peak at potentials of about 0.60−0.63 V (Fig. 7A,B). It is noted that increasing alcohol concentration caused a slight shift of these maxima towards more positive potentials. Compared to the Ni wire electrode, the nanostructured catalysts have both significantly increased specific and mass activities (Table 3). Considering the abundance of Ni, the mass activity is of minor importance, while the improved specific activities and the high surface area in the case of the intensely roughened, hydrazine-reduced Ni NTs are relevant benefits of the presented catalyst systems.

To quantify the additional currents corresponding to the alcohol oxidation, the current densities of the Ni structures in pure sodium hydroxide electrolyte during the voltage cycling were subtracted from those recorded in the presence of EtOH. Fig. 8 shows the

Fig. 8. Background-corrected EtOH-induced currents with respect to the EtOH-free reference experiments. The lines denote the linear extrapolation of the current increase in the presence of 0.05 mol L^{-1} EtOH. A) Ni—B NT catalyst. B) Ni NT catalyst. C) Ni wire catalyst as reference.

nanowires [14,44] indicates that these highly anisotropic, unsupported metal electrocatalysts can be very aging-resistant, probably because typical degradation mechanisms such as support corrosion, loss of electrical contact or particle agglomeration do not apply to them or at least are less pronounced. Due to the passivation of Ni in alkaline environment, metal dissolution is also an unprobable degradation path. However, the NT structures may be subject to detrimental morphological and compositional changes in long-term operation, e.g. fragmentation or oxidation.

4. Conclusions

The newly developed electroless plating bath gives access to intensely roughened thin films and derived, complex shaped structures consisting of nanocrystalline, pure Ni. Compared to borane-based depositions, both the purity and the increased surface area of the deposit are interesting for potential catalytic applications. As confirmed by the fabrication of high aspect-ratio Ni and Ni—B NTs and their application in the oxidation of EtOH, electroless plating is a powerful route towards unsupported Ni nanostructures with electrocatalytic properties which can outperform the corresponding bulk materials. In this reaction, the presence of boron did not hamper the catalyst performance.

Considering the low synthetic effort, the pronounced flexibility and good scalability of electroless plating in combination with the excellent activity of the obtained products, the presented results are valuable for the development of direct alcohol fuel cells. In addition to the possible applications in synthetic (electro)chemistry and energy generation, the improved linearity of the synthesized catalysts demonstrates their potential in sensing technology.

The utilization of promoting elements can be a promising route for further performance enhancements. In combination with the versatile applicability of Ni, the vast range of synthetic approaches towards binary or multimetallic systems provides many prospects for future research.

References

[1] A. Boddien, D. Mellmann, F. Gärtner, R. Jackstell, H. Junge, P.J. Dyson, G. Laurenczy, R. Ludwig, M. Beller, Science 333 (2011) 1733—1736.
[2] B. Filanovski, E. Granot, R. Dirawi, I. Presman, I. Kuras, F. Patolsky, Nano Lett. 11 (2011) 1727—1732.
[3] K.L. Nagashree, M.F. Ahmed, J. Solid State Electrochem. 14 (2010) 2307—2320.
[4] Z. Liu, Z. Li, F. Wang, J. Liu, J. Ji, J. Wang, W. Wang, S. Qin, L. Zhang, Mater. Lett. 65 (2011) 3396—3398.
[5] N.R. Stradiotto, K.E. Toghill, L. Xiao, A. Moshar, R.G. Compton, Electroanalysis 21 (2009) 2627—2633.
[6] X. Tian, X. Zhao, L. Zhang, C. Yang, Z. Pi, S. Zhang, Nanotechnology 19 (2008) 215711.
[7] G. Jin, Y. Ding, P. Zheng, J. Power Sources 166 (2007) 80—86.
[8] Y. Liu, H. Teng, H. Hou, T. You, Biosens. Bioelectron. 24 (2009) 3329—3334.
[9] E. Antolini, Energy Environ. Sci. 2 (2009) 915—931.
[10] E. Antolini, E.R. Gonzalez, J. Power Sources 195 (2010) 3431—3450.
[11] E. Antolini, J. Perez, J. Mater. Sci. 46 (2011) 4435—4457.
[12] Z. Chen, M. Waje, W. Li, Y. Yan, Angew. Chem. Int. Ed. 46 (2007) 4060—4063.
[13] C. Cui, H. Li, S. Yu, Chem. Sci. 2 (2011) 1611—1614.
[14] S.M. Choi, J.H. Kim, J.Y. Jung, E.Y. Yoon, W.B. Kim, Electrochim. Acta 53 (2008) 5804—5811.
[15] W. Wang, N. Li, X. Li, W. Geng, S. Qiu, Mater. Res. Bull. 41 (2006) 1417—1423.

systems, the boron content does not disturb the EtOH oxidation (in contrast to other reaction types such as hydrogenations [22]). This result is in accordance with the effective oxidation of uric acid on Ni catalysts obtained by sodium borohydride reduction [41] and a similar activity of electrodes composed of polycrystalline Ni and an amorphous, B-containing Ni alloy in EtOH electrooxidation [42]. Considering the Ni NTs, the high surface roughness (Fig. 2) is an additional benefit in heterogeneous (electro)catalysis when considering total instead of normalized activities.

Although this study did not cover the long term stability of the Ni structures, related work on metal NTs [12,43] and metal

[16] I. Enculescu, M. Sima, M. Enculescu, E. Matei, M.E. Toimil Molares, T. Cornelius, Optoelectron. Adv. Mater. Rapid Commun. 2 (2008) 133–136.

[17] F. Muench, M. Oezaslan, T. Seidl, S. Lauterbach, P. Strasser, H.-J. Kleebe, W. Ensinger, Appl. Phys. A 105 (2011) 847–854.

[18] F. Formanek, N. Takeyasu, T. Tanaka, K. Chiyoda, A. Ishikawa, S. Kawata, Appl. Phys. Lett. 88 (2006) 083110.

[19] P. Steinmetz, S. Alperine, A. Friant-Costantini, P. Josso, Surf. Coatings Technol. 43/44 (1990) 500–510.

[20] M.Z. Figueroa-Torres, L. De la torre Sáenz, C. Domínguez Ríos, R. Torres-Sánchez, A. Aguilar-Elguézabal, Top. Catal. 54 (2011) 568–571.

[21] F. Muench, M. Rauber, C. Stegmann, S. Lauterbach, U. Kunz, H.-J. Kleebe, W. Ensinger, Nanotechnology 22 (2011) 415602.

[22] Z. Wu, S. Ge, M. Zhang, W. Li, S. Mu, K. Tao, J. Phys. Chem. C 111 (2007) 8587–8593.

[23] S. Arai, Y. Imoto, Y. Suzuki, M. Endo, Carbon 49 (2011) 1484–1490.

[24] E. Ferain, R. Legras, Nucl. Instrum. Methods Phys. Res. B 208 (2003) 115–122.

[25] A.G. Pshenichnikov, L.A. Burkal'tseva, Z.I. Kudryavtseva, Electrochim. Acta 45 (2000) 4143–4150.

[26] S. Haag, M. Burgard, B. Ernst, Surf. Coat. Technol. 201 (2006) 2166–2173.

[27] G. Wen, Z.X. Guo, C.K.L. Davies, Scripta Mater. 43 (2000) 307–311.

[28] S. Arai, M. Kobayashi, T. Yamamoto, M. Endo, Electrichim. Solid State Lett. 13 (2010) D94–D96.

[29] I. Ohno, O. Wakabayashi, S. Haruyama, J. Electrochem. Soc. 132 (1985) 2323–2330.

[30] H. Mukaibo, L.P. Horne, D. Park, C.R. Martin, Small 21 (2009) 2474–2479.

[31] W. Xing, S. Qiao, X. Wu, X. Gao, J. Zhou, S. Zhuo, S.B. Hartono, D. Hulicova-Jurcakova, J. Power Sources 196 (2011) 4123–4127.

[32] K.S. Kim, W.E. Baitinger, J.W. Amy, N. Winograd, J. Electron. Spectrosc. Relat. Phenom. 5 (1974) 351–367.

[33] J. Liu, H. Zhou, Q. Wang, F. Zeng, Y. Kuang, J. Mater. Sci. 47 (2012) 2188–2194.

[34] J.-H. Shen, Y.-W. Chen, J. Mol. Catal. A: Chem. 273 (2007) 265–276.

[35] Y.N. Bekish, T.V. Gaevskaya, L.S. Tsybulskaya, G.-Y. Lee, M. Kim, Prot. Met. Phys. Chem. Surf. 46 (2010) 325–331.

[36] J.F. Moulder, W.F. Stickle, P.E. Sobol, K.D. Bomben, Handbook of X-ray Photoelectron Spectroscopy, Physical Electronics Inc., Eden Prairie (Minnesota), 1995.

[37] M.A. Sattar, B.E. Conway, Electrochim. Acta 14 (1969) 695–710.

[38] M. Fleischmann, K. Korinek, D. Pletcher, J. Electroanal. Chem. 31 (1971) 39–49.

[39] P.K. Shen, Z. Yan, H. Meng, M. Wu, G. Cui, R. Wang, L. Wang, K. Si, H. Fu, RSC Adv. 1 (2011) 191–198.

[40] N.M. Suleimanov, S.M. Khantimerov, E.F. Kukovitsky, V.L. Matukhin, J. Solid State Electrochem. 12 (2008) 1021–1023.

[41] B. Singh, F. Laffir, C. Dickinson, T. McCormac, E. Dempsey, Electroanalysis 23 (2011) 79–89.

[42] T. Kessler, A.M. Castro Luna, Int. J. Res. Phys. Chem. Chem. Phys. 185 (1994) 79–90.

[43] S.M. Alia, G. Zhang, D. Kisailus, D. Li, S. Gu, K. Jensen, Y. Yan, Adv. Funct. Mater. 20 (2010) 3742–3746.

[44] H.-W. Liang, X. Cao, F. Zhou, C.-H. Cui, W.-J. Zhang, S.-H. Yu, Adv. Mater. 23 (2011) 1467–1471.